

Topological edge and corner states of valley photonic crystals with zipper-like boundary conditions

Yun-Feng Shen(沈云峰), Xiao-Fang Xu(许孝芳), Ming Sun(孙铭), Wen-Ji Zhou(周文佶), and Ya-Jing Chang(常雅箐)

Citation: Chin. Phys. B, 2024, 33 (**4**): 044203. DOI: 10.1088/1674-1056/ad1e6a
Journal homepage: http://cpb.iphy.ac.cn; http://iopscience.iop.org/cpb

What follows is a list of articles you may be interested in

Tailoring topological corner states in photonic crystals by near- and far-field coupling effects

Zhao-Jian Zhang(张兆健), Zhi-Hao Lan(兰智豪), Huan Chen(陈欢), Yang Yu(于洋), and Jun-Bo Yang(杨俊波)
Chin. Phys. B, 2023, 32 (**12**): 124201. DOI: 10.1088/1674-1056/acddd3

Topological states switching and group velocity control in two-dimensional non-reciprocal Hermitian photonic lattice

Yu Lin(林宇), Yuandan Wang(王元旦), Junhao Yang(杨俊豪), Yixuan Fu(符艺萱), and Xinyuan Qi(齐新元)
Chin. Phys. B, 2023, 32 (**11**): 114213. DOI: 10.1088/1674-1056/ad0621

Topological resonators based on hexagonal-star valley photonic crystals

Xin Wan(万鑫), Chenyang Peng(彭晨阳), Gang Li(李港), Junhao Yang(杨俊豪), and Xinyuan Qi(齐新元)
Chin. Phys. B, 2023, 32 (**11**): 114208. DOI: 10.1088/1674-1056/acf44b

High-performance chiral all-optical OR logic gate based on topological edge states of valley photonic crystal

Xiaorong Wang(王晓蓉), Hongming Fei(费宏明), Han Lin(林瀚), Min Wu(武敏), Lijuan Kang(康丽娟), Mingda Zhang(张明达), Xin Liu(刘欣), Yibiao Yang(杨毅彪), and Liantuan Xiao(肖连团)
Chin. Phys. B, 2023, 32 (**7**): 074205. DOI: 10.1088/1674-1056/accb41

Topological phases and type-II edge state in two-leg-coupled Su-Schrieffer-Heeger chains

Tianqi Luo(罗天琦), Xin Guan(关欣), Jingtao Fan(樊景涛), Gang Chen(陈刚), and Suo-Tang Jia(贾锁堂)
Chin. Phys. B, 2022, 31 (**1**): 014208. DOI: 10.1088/1674-1056/ac3650

Topological edge and corner states of valley photonic crystals with zipper-like boundary conditions

Yun-Feng Shen(沈云峰)[1], Xiao-Fang Xu(许孝芳)[1,2,†], Ming Sun(孙铭)[1], Wen-Ji Zhou(周文佶)[1], and Ya-Jing Chang(常雅箐)[1]

[1] *School of Mechanical Engineering, Jiangsu University, Zhenjiang* 212000, *China*
[2] *School of Optical and Electronic Information, Suzhou City University & Suzhou Key Laboratory of Biophotonics, Suzhou* 215104, *China*

(Received 17 November 2023; revised manuscript received 11 January 2024; accepted manuscript online 15 January 2024)

We present a stable valley photonic crystal (VPC) unit cell with C_{3v} symmetric quasi-ring-shaped dielectric columns and realize its topological phase transition by breaking mirror symmetry. Based on this unit cell structure, topological edge states (TESs) and topological corner states (TCSs) are realized. We obtain a new type of wave transmission mode based on photonic crystal zipper-like boundaries and apply it to a beam splitter assembled from rectangular photonic crystals (PCs). The constructed beam splitter structure is compact and possesses frequency separation functions. In addition, we construct a box-shaped triangular PC structures with zipper-like boundaries and discover phenomena of TCSs in the corners, comparing its corner states with those formed by other boundaries. Based on this, we explore the regularities of the electric field patterns of TESs and TCSs, explain the connection between the characteristic frequencies and locality of TCSs, which helps better control photons and ensures low power consumption of the system.

Keywords: valley photonic crystal, topological edge states, topological corner states, higher-order topological insulators, topological phase transition

PACS: 42.70.Qs, 03.65.Vf, 42.25.Bs, 42.81.Dp **DOI:** 10.1088/1674-1056/ad1e6a

1. Introduction

Topological insulators are considered to be highly promising materials due to their self-insulating but transportable properties at boundaries. Topology is a mathematical concept that describes the shape and structure of spaces. Researchers drew inspiration from the mechanisms of topological insulators and introduced the concept of topology into photon systems, leading to the proposal of photonic crystals (PCs) that enable unidirectional propagation of electromagnetic waves along specific pathways. Scholars, based on extensive studies of the band theory of topological insulators, have realized phenomena such as the quantum Hall effect (QHE),[1] Quantum spin Hall effect (QSHE),[2] and quantum valley Hall effect (QVHE).[3–5] QVHE can be achieved by introducing valley degrees of freedom and easier to construct and implement compared to QHE and QSHE, thus allowing for a richer diversity in structural shapes.[6,7] Since the wave functions in photonic crystals are analogous to the wave functions of electrons in condensed matter physics systems, various phenomena observed in the field of condensed matter physics, such as QSHE and QVHE, can be realized in wave systems.[7] This approach has led to numerous applications of QSHE and QVHE in research of photonic crystals, rapidly emerging as prominent fields and bringing vitality to the development of photonic crystals.

Valley photonic crystals (VPCs) have attracted great interest not only for their inherent properties of traditional photonic crystals but also for their valley polarization characteristics.[8–11] People can achieve the double degeneracy at the K or K' points by breaking the spatial inversion symmetry of the hexagonal unit cell lattice.[12–15] Numerous methods can be used to realize VPCs, such as lattice deformation and the use of tunable dielectric materials.[16,17] However, more stable cell structures and properties, as well as wider bandgap widths, remain the anchors and objectives of research. Therefore, it is necessary to explore new structures and topological transitions to achieve VPCs. VPCs systems also face issues such as defects, interference, and losses. To address these problems, it is essential to ensure the controllability and low power consumption of the VPCs system. Topological edge states (TESs) and topological corner states (TCSs) are effective methods for controlling photons and ensuring the system's low power consumption.[18]

There has been much research on topological edge states. From the literature, it is known that devices such as optical waveguides, beam splitters, filters, and resonators have been designed based on the excellent backscattering immunity and robustness of topological edge states.[18–21] If the edge states possess topological protection, these states are strongly confined between topological photonic crystals with different topological phases. The transmission of topological edge states exhibits robustness and lacks backward scattering, allowing for resilient propagation at interfaces with defects. Due to the robustness of topology-protected transport, sharp bends

[†]Corresponding author. E-mail: xiaofangxu@aliyun.com

© 2024 Chinese Physical Society and IOP Publishing Ltd

of 120° and 60° are applied in these device applications and have a high transmission rate. However, there has not been much research on 90° sharp bends. Due to the backscattering immunity and robustness of VPCs, changing the boundary stitching structure on the basis of edge states does not affect the transmission, so the domain wall morphology of boundaries is highly malleable.[22–24] To meet various applications and real manufacturing needs, simpler, more stable, and practical high-transmission-efficiency boundaries await further exploration.

In recent years, higher-order topological insulators (HOTIs) have been introduced into photonic systems to realize TCSs.[25–29] TCSs, unlike edge states studied previously, where the energy is distributed at the stitched edges of photonic crystal structures with different topological phases, are low-dimensional states protected by bulk band topology that are confined to the corners of a structure. Energy is well confined to a point or several points under regular conditions.[7,30] Therefore, it can be seen as a new way to manipulate electromagnetic waves and is also considered a powerful approach to developing new cavity modes and optical devices.

In 2021, Phan *et al.* designed a box-shaped structure where one PC is embedded into another, realizing corner states at the 60° corners of the zigzag-type boundary between the two PCs. At the 60° corner, the sign of the valley Chern number flips, and TCSs appear.[31,32] In addition, most other studies on TCSs using hexagonal lattice realizations have only examined corner structures of PCs constituted by zigzag-type boundary bends,[33,34] and more shapes of topological corner structures have not been widely studied. Further exploration of the changes and impacts of different edge domain walls and corner structures on TCSs, understanding the information conveyed by TCSs characteristic frequencies, is of significant investigational importance and greatly aids in constructing new devices based on TCSs.

In this paper, we propose a valley photonic crystal composed of a quasi-ring-shaped dielectric column with C_{3v} symmetry, which possesses C_{3v} symmetry by rotating the quasi-ring-shaped dielectric column to break its mirror symmetry. When the mirror symmetry at the K (K') point is broken, band degeneracy is lifted, and a bandgap emerges near the degeneracy point. The frequency range of the topological bandgap is from $0.2583c/a$ to $0.3364c/a$, where a is the lattice constant and c is the speed of light in free space. The bandgap between the energy bands of the proposed unit cell is wider than that of the quasi-ring-shaped structures with other differences in inner and outer diameters, and the single-cell property has stronger anti-interference characteristics. The quasi-ring-shaped structure we propose can achieve edge states, proving that valley edge states with topological protection can propagate along interfaces with sharp bends and defects. On this basis, a mode of electromagnetic wave propagation on a zipper-like boundary is obtained, where the electromagnetic wave can propagate in a spiral shape along 90° with high quality. Based on the excellent transmission properties of this propagation mode, we construct a simple and convenient three-output structure composed of four rectangular photonic crystal modules, achieving good beam-splitting and frequency-division effects. In addition, combining VPCs with different topological phases in different ways will lead to different TESs and TCSs in the combined structure. We construct a box-shaped triangular structure where one VPC wraps another VPC. We explore the differences in TCSs when the contact interface structures of the two VPCs are zigzag-shaped boundaries and zipper-like boundaries. The box-shaped structure with a zipper-like boundary has a novel 60° angular structure, where a larger number of TCSs was found at the corner. Through these studies, we achieve new TCSs and explore the transition between TCSs and TESs, as well as the association between the characteristic frequencies of TCSs and their locality. These findings can be applied to topological devices, such as topological lasers and topological resonators.

2. Theory and model

As shown in Fig. 1(a), we center the concentric circular annular dielectric columns and cut them evenly into six segments at 60° per section, selecting three segments to form the dielectric columns, which are the green parts in Fig. 1(a). Figure 1(b) shows the valley photonic crystal unit cell of the quasi-ring-shaped dielectric column with C_{3v} symmetry we propose. In the structure, the inner radius of the annulus is R_1, and the outer radius is R_2. The material of the dielectric column is silicon (dielectric constant $\varepsilon_1 = 11.7$), and the white background in Fig. 1 represents air (dielectric constant $\varepsilon_0 = 1$). We arrange the cells as shown in Fig. 1(c), with a lattice constant of 1000 nm.

In this paper, we study two-dimensional (2D) dielectric column topological photonic crystals (PhCs), considering only their TM[35,36] modes. The Hamiltonian of the valley photonic crystals can be determined based on the specific system and structure. According to perturbation theory, the effective Hamiltonian of the system is expressed as[10,37]

$$\hat{H} = v_{\mathrm{D}}(\hat{\sigma}_x\hat{\tau}_z\delta k_x + \hat{\sigma}_y\delta k_y) + \omega_{\mathrm{D}}\Delta P\hat{\sigma}_z, \tag{1}$$

where v_{D} is the Dirac velocity, δk_x and δk_y are the reciprocal vector components measured from the K or K' valleys, $\hat{\tau}_z$ and $\hat{\sigma}_x$ are the Pauli matrices acting on the valley and sublattice spaces, respectively, and ΔP is the perturbation strength. The size of the energy gap is $\Delta\omega = 2\omega_{\mathrm{D}}|\Delta P|$, where ω_{D} is the Dirac frequency.

Regarding valley photonic crystals, one can traditionally transform a photonic structure with C_{6v} symmetry into one

with C_3 symmetry by breaking spatial inversion symmetry.[35] In addition to the above method, as we know, spatial inversion symmetry can also be broken by moving the dielectric pillars in a photonic structure with C_3 symmetry. By changing the distance between the dielectric pillars and the center of the unit cell, the Wannier centers in the photonic crystal are affected, thereby adjusting the degree of inter-cell/intra-cell coupling in the structure to achieve a topological phase transition, open a band gap, and also realize valley photonic crystals.[30,32]

This paper uses the eigenfrequency analysis of COMSOL Multiphysics and the finite element method to numerically solve for the dispersion relations. We break the mirror symmetry of the C_{3v} symmetric valley photonic crystals by rotating the unit cell structure of the C_{3v} symmetric valley photonic crystals to transform it into a C_3 symmetric photonic crystal unit cell structure, which can also realize valley photonic crystals. The most important hallmark of C_{3v} symmetry is that the unit cell structure at the K or K' points in momentum space also has mirror symmetry.[7] As shown in Fig. 1(c), the rotation of the dielectric pillars in the C_{3v} symmetric photonic structure around the center of the circle as the rotational axis is depicted, with the rotation angle denoted as θ. When $\theta = 30°$, the unit cell structure is called VPC1, and when $\theta = -30°$, it is called VPC2. During the rotation, the mirror symmetry is broken, and the band gap of the photonic crystal is opened.

When a unit cell at the K or K' point in momentum space, as shown in Fig. 1(e), has mirror symmetry, the structure exhibits C_{3v} symmetry. Therefore, by rotating the silicon dielectric pillars, we actually change the mirror symmetry at the K or K' points. For instance, in Fig. 1(c), when $\theta = 0°$, there is mirror symmetry at the K, K' points, and the structure in momentum space exhibits C_{3v} symmetry. When θ is not equal to 0°, the mirror symmetry at K and K' is broken, and the structure becomes C_3 symmetric. However, when the dielectric columns are rotated by 60°, its structure is the same as the initial state at 0°. According to this rule, every time the dielectric columns are rotated by 60°, the structure will again exhibit C_{3v} symmetry. Thus, for the unit cell structure proposed in this paper, mirror symmetry occurs at each rotation angle equal to $n\pi/3$ (where n is an integer).

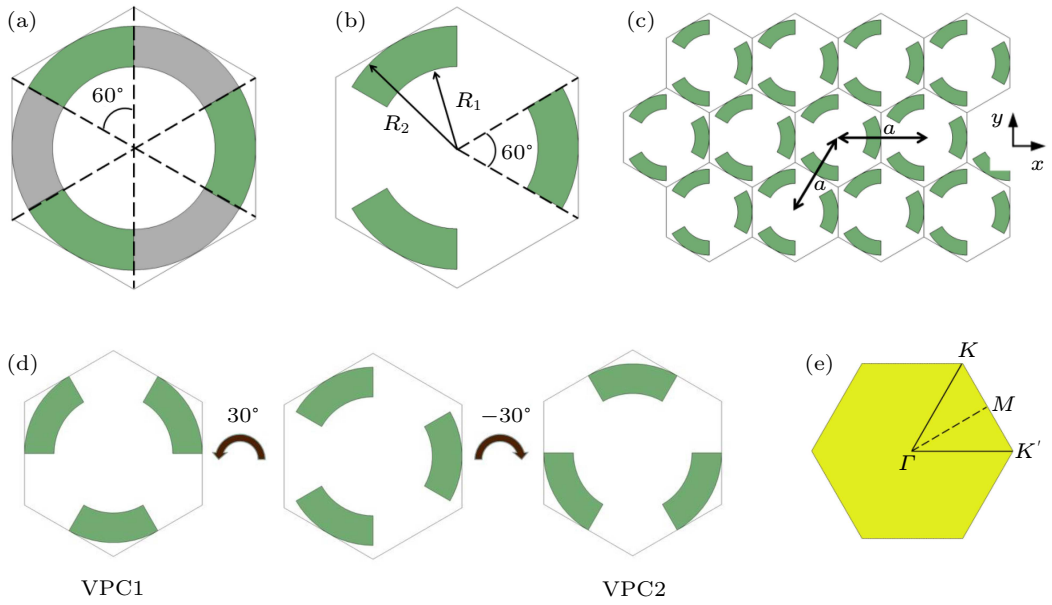


Fig. 1. (a) The torus is evenly divided into six segments by cutting every 60°, and three of them are taken as silicon dielectric columns. (b) The quasi-ring-shaped valley photonic crystal cell structure constructed in this paper, where the outer radius is $R_2 = 0.5a$ and the inner radius is $R_1 = a/3$. (c) The quasi-ring-shaped PC composed of quasi-torus valley photonic crystal cells, where a is the lattice constant of 1000 nm. (d) The quasi-ring-shaped dielectric columns are rotated by 30° and −30° respectively to obtain VPC1 and VPC2. (e) The momentum space of the unit cell, with the first Brillouin regions of the highly symmetric points K, K', Γ, and M.

The topological phase transition of the unit cell can be characterized by the valley Chern number. We calculate the valley Chern number for the first band by integrating the local Berry curvature derived from the effective Hamiltonian, and the valley Chern number can be used to represent the topological properties of the VPC system. The valley Chern numbers for the first band at points K and K' are[38]

$$C_{K/K'} = \frac{1}{2\pi} \int_{\mathrm{HBZ}} \Omega_{K/K'}(k) \mathrm{d}^2 k, \tag{2}$$

where $\Omega_{K/K'}(k)$ represents the local Berry curvature, and the integration is performed over half the Brillouin zone (HBZ) surrounding the K/K' valleys. A direct method to compute the Chern number involves replacing all derivatives with discrete differences and integrals with summations. The Berry curvature $\Omega_{K/K'}(k)$ can be efficiently computed using an efficient algorithm, which involves summing the phases of the electric field E_k in the discretized k-space[39]

$$\Omega_{K/K'}(k) = \nabla_k \times \mathrm{i}\langle E_k | \nabla_k E_k \rangle. \tag{3}$$

The aforementioned calculations are carried out using first-principles methods for computing the Berry curvature and Chern numbers. However, we can also proceed to estimate the valley Chern numbers[37] according to

$$C_{K/K'} = \frac{1}{2}\mathrm{sgn}(\Delta P_{(K/K')}). \tag{4}$$

When calculating the valley Chern number, the term ΔP represents the strength of perturbation arising from geometric disturbances that break mirror symmetry. ΔP is directly proportional to the bandwidth between the first and second bands ($2v_{\mathrm{D}}|\Delta P|$). We can give the specific calculation formula for ΔP as follows:

$$\begin{aligned} 2\Delta P &\equiv \Delta^{\mathrm{RR}}_{P,K/K'} - \Delta^{\mathrm{LL}}_{P,K/K'} \\ &= -\int_{\mathrm{V}} \Delta\varepsilon(r_\perp)\cdot\left(|e^{\mathrm{R}}_\perp|^2 - |e^{\mathrm{L}}_\perp|^2\right)\mathrm{d}V. \end{aligned} \tag{5}$$

However, due to the nature of the sgn function, the numerical value of the valley Chern number is solely determined by the $\pm$ sign of ΔP. The $\pm$ sign of ΔP depends on whether the vacuum region is replaced by Si. In this paper, ΔP for VPC2 is negative, while ΔP for VPC1 is positive. When ΔP is negative, $C_K = -1/2$ and $C_{K'} = 1/2$ for VPC1. When ΔP is positive, $C_K = 1/2$ and $C_{K'} = -1/2$ for VPC2. The opposite signs of the valley Chern numbers for them indicate that there is a topological phase transition in the structure upon rotation, and VPC1 and VPC2 exhibit different non-trivial topological phases. This conclusion is supported by the phase inversion at points K and K' shown in Fig. 2(d). We can then calculate the topological invariant $C_{\mathrm{v}} = C(K) - C(K')$. The difference in topological indices between VPC1 and VPC2 in the K or K' valleys can be denoted as[8,10,37]

$$\Delta C_{K/K'} = C^{\mathrm{VPC1}}_{K/K'} - C^{\mathrm{VPC2}}_{K/K'} = \pm 1. \tag{6}$$

According to the edge state theory, a topological edge state can appear at the boundary between two VPCs with different valley Chern numbers. Under the condition of applying a circularly polarized light source at the domain wall between the VPC1 and VPC2 domains, it is possible to observe the unidirectional edge state transmission protected by topology.

The first Brillouin zone (FBZ) in the lattice is defined at its vertices as the K and K' points, which are known as valley points, as shown in Fig. 1(d). We set three pairs of periodic boundary conditions on the edges of the hexagonal unit cell and then scanned the wave vector in the first Brillouin zone to obtain the band structures of VPC1, the C_{3v} symmetric unit cell and VPC2.

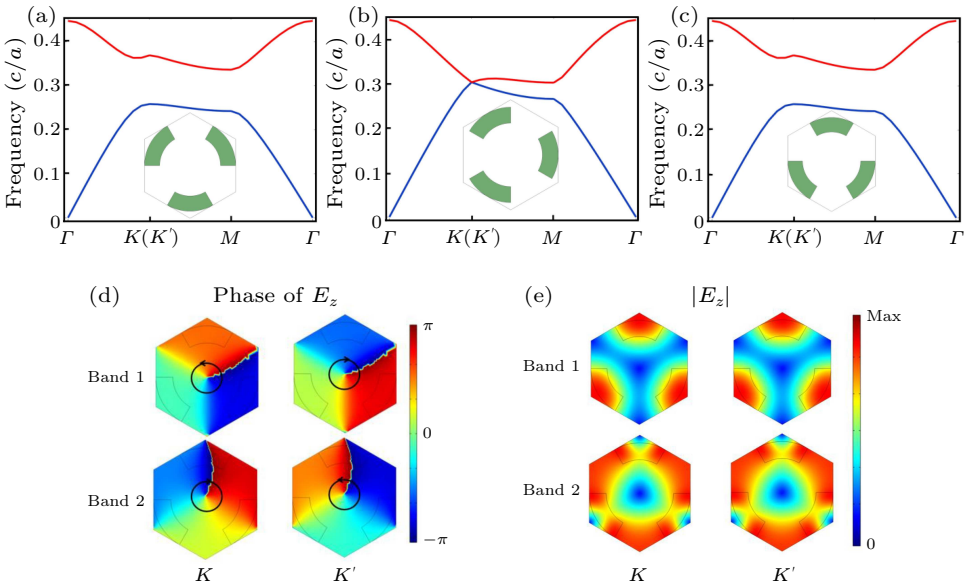


Fig. 2. (a)–(c) The band structures of VPC2, C_{3v} symmetric unit cell, and VPC1, respectively. (d) The phase distribution of the two bands of VPC2 at K and K' points. (e) The electric field distribution of the two bands of VPC2 at K and K' points.

In Fig. 2(b), we can see that the structure is C_{3v} symmetric at $\theta = 0°$. Dirac cones appear at the K (K') points in the band diagram, while at $\theta = 30°$ or $\theta = -30°$, the band structures of VPC1 and VPC2 open a clear bandgap at K (K'), and the bandgaps of VPC1 and VPC2 are almost the same. Therefore, we know that the two bands of the C_{3v} symmetric unit cell are degenerated at the Dirac point. By rotating the quasi-circular dielectric columns, we reduce the symmetry of the structure to C_3 symmetry, breaking the mirror symmetry, and opening the Dirac point in the band diagram.

We analyze the phase and amplitude distribution of electric field E_z at K (K') for VPC2. In Fig. 2(e), the color represents the amplitude of the E_z component, and we can observe a phase reversal, indicating a topological phase transition. At the same time, in the phase distribution diagram of the VPC2 unit cell structure shown in Fig. 2(d), we find that within the

same band, K and K' possess opposite vortex chiralities, which are represented by the clockwise and counterclockwise black arrows in the diagram. They describe the right circularly polarized (RCP) and left circularly polarized (LCP) orbital angular momenta, respectively, and also indicate that band inversion is present, suggesting a topological phase transition in this valley photonic crystal.

We analyze the effects on the unit cell due to the variation of the difference between the inner and outer radii (represented in this paper as $\Delta_x - \Delta_0$). Here $\Delta_0 = R_2 - R_1$, and $\Delta_x = R_2' - R_1'$ indicates the difference between the inner and outer radii after the change. As shown in Fig. 3(a), the frequency of the Dirac point, ω_D, increases as $\Delta_x - \Delta_0$ increases. Consequently, the bandgap that opens after the Dirac point also shifts upward. We know that the TESs and TCSs realized by a photonic crystal cannot exceed the bandgap range of the unit cell. Based on this conclusion, we can adjust the unit cell's bandgap by modifying the difference between the inner and outer radii, thereby controlling the operational frequency bands of TCSs and TESs.

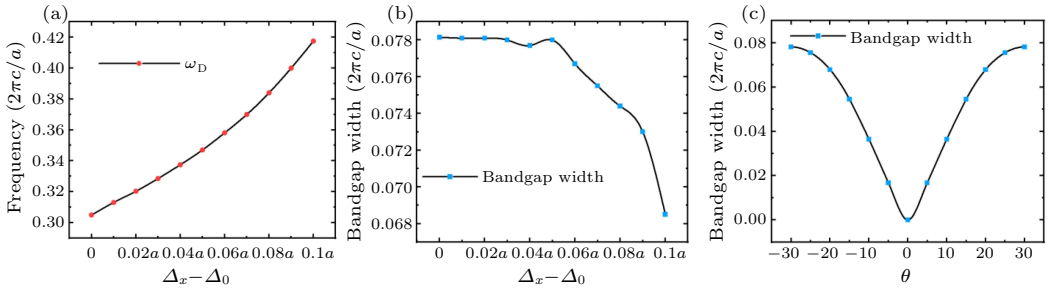


Fig. 3. (a) The variation of frequency of the Dirac cone with the difference in the radius of the inner and outer circles of the dielectric column. (b) The variation of band gap width with the difference in the radius of the inner and outer circles of the dielectric column. (c) The variation of band gap width with the rotation angle of the dielectric column.

Figure 3(b) illustrates how the bandgap width varies with the difference between the outer and inner diameters. The larger the $\Delta_x - \Delta_0$, the smaller the bandgap. When the difference between the inner and outer radii is between 0 and $0.5a$, the width of the bandgap remains almost unchanged, which implies that minor perturbations concerning the inner and outer radii have a negligible effect on the bandgap, indicating the unit cell's robustness against disturbances in the diameters of the dielectric columns. In combination with Fig. 3(a), the unit cell structure, when the difference between the outer and inner radii is small, only changes the frequency of the operational band without altering the bandwidth, making it relatively easy to control. However, when $\Delta_x - \Delta_0$ exceeds $0.5a$, the perturbation has a significant impact on the unit cell, that is, the perturbation causes considerable changes in both the operational frequency and the bandwidth, which are difficult to control. Therefore, the difference between the inner and outer radii of such structures should ideally be kept less than $0.5a$.

Based on the theory discussed above, we know that the mirror symmetry of the K or K' point can be altered by rotation, thereby opening a bandgap. However, the influence of each rotation angle on the bandgap is different. Figure 3(c) shows the bandgap under various rotation angles. It is evident that when the rotation angle is in the ranges from $-30°$ to $-20°$ and from $20°$ to $30°$, the bandgap is wider. Moreover, within these ranges, the bandgap varies less with the rotation angle, indicating a stronger ability of the unit cell to resist the impact of rotation. Outside this range, the bandgap width shows a sharp downward trend. Therefore, the rotational error of the structure should fall within the ranges from $-30°$ to $-20°$ and from $20°$ to $30°$.

Through the analysis of structural data, we have identified the optimal structure, that is, the quasi-ring-shaped dielectric pillar structure with $R_2 - R_1 = \Delta_0$ when rotated by $\pm 30°$, as used in this article. This choice maximizes the robustness of the unit cell structure at the single-cell level, meaning that the single-cell structure can retain its performance to the greatest extent when subjected to minor disturbances or errors.

3. Topological valley photonic crystal edge states

We combine VPC1 and VPC2 to form supercell structures as shown in Figs. 4(a) and 4(b), arranging the hexagonal cells of VPC1 and VPC2 at the boundary in edge-1 and edge-2 configurations. The upper and lower boundaries of the supercell are set as perfect electric conductor boundary conditions, and the left and right boundaries are set as periodic boundary conditions. VPC1 is depicted with red structures, while VPC2 is shown with blue. The boundary with VPC1 on top and VPC2 at the bottom is called the edge-1 type, and the one with VPC2 on top and VPC1 at the bottom is called the edge-2 type, both of which have a zigzag boundary. The band structures of the two supercells are shown in Figs. 4(c) and 4(d), where the black dashed lines represent bulk states, and we can observe edge states formed at the boundaries between the bulk states. The edge modes depicted by the blue and red solid lines respectively represent the valley pseudospin states of the supercell structures in Figs. 4(a) and 4(b). In Figs. 4(c)

and 4(d), the edge modes represented by the blue solid lines have two different valley pseudospin states, denoted as Φ_{12}^{+} and Φ_{12}; for one of the edge modes represented by the red solid lines, it also have two different valley pseudospin states, namely Φ_{21}, and Φ_{21}^{+}. Figures 4(e) and 4(f) display the electric field E_z diagrams and Poynting vectors of different valley pseudospin states, which allow us to analyze the behavior of the energy flow. We find that energy is primarily concentrated at the boundaries. Among them, the energy flows of Φ_{12}^{+} and Φ_{12} are opposite, similar to the energy flows of Φ_{21} and Φ_{21}^{+}.

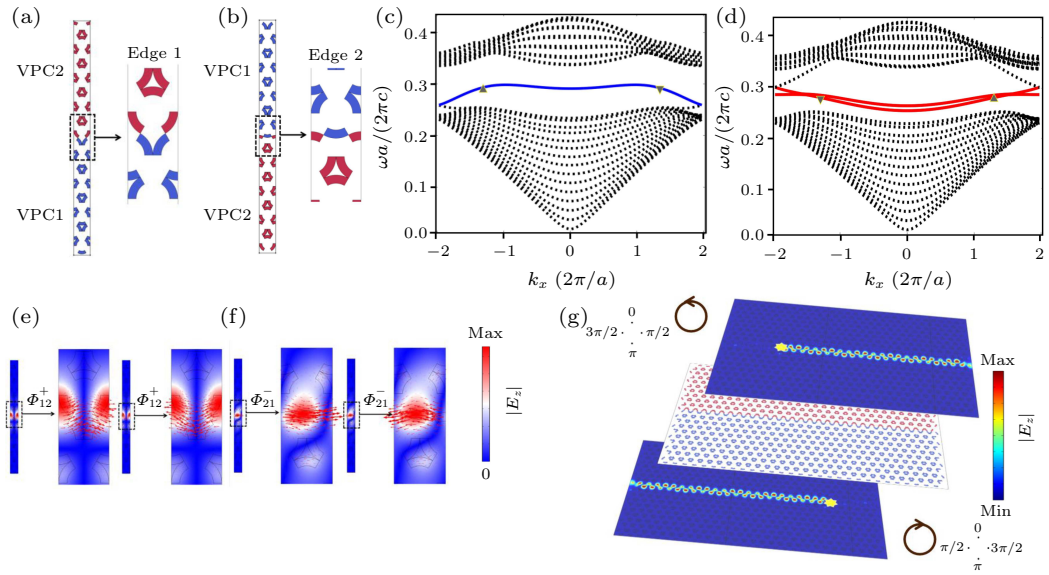


Fig. 4. Topological edge states of valley photonic crystals. [(a), (b)] Two differently arranged supercell structures. In (a), VPC2 is on top, and VPC1 is at bottom, and we refer to the structure at the interface as the edge-1 structure. In (b), VPC1 is on top, and VPC2 is at bottom, with the interface being the edge-2 structure. [(c), (d)] The band structures for supercells (a) and (b), respectively. (e) The electric field distribution and Poynting vector diagram for the supercell edge-1. (f) displays the electric field distribution and Poynting vector diagram for the supercell edge-2. (g) The E_z field distribution of the straight waveguide when excited with RCP and LCP chiral sources.

To verify the valley chirality of the valley Hall effect, we place an orbital angular momentum (OAM) harmonic source at the boundary between VPC1 and VPC2. The harmonic source is composed of four line sources with a phase difference of $\pi/2$, which can excite valley chirality when the orbital angular momentum is positive or negative. This can also be referred to as a chiral source. Electromagnetic waves propagate along the boundaries of VPC1 and VPC2. By using the harmonic source and controlling the polarization direction of the source, we can achieve the quantum valley Hall effect. We also set a layer of perfect electric conductor boundary conditions around the model to prevent electromagnetic waves from scattering outward. As shown in Fig. 4(g), when the harmonic source carries a positive OAM ($L=-1$), corresponding to LCP (left circular polarization), the electric field distribution indicates that the electromagnetic waves propagate to the right along the zigzag boundary, with no significant backscattering. The electromagnetic waves transmit near the boundary without scattering into the interiors of the two VPC domains, exhibiting good optical localization. When the harmonic source carries a negative OAM ($L=1$), corresponding to RCP (right circular polarization), we can observe the electromagnetic waves propagating in the opposite direction with the same nature and state. Through the simulation study of supercells with both types of boundary structures, we find that the valley-polarized edge states located at the K or K' points propagate only in one direction along the boundary, which demonstrates the valley chirality characteristic of the valley Hall effect.

The band diagram analysis of the supercell presented in this article shows that there is TES transmission when the structure is spliced according to edge-1 and edge-2 types. As shown in Fig. 4(g) for the defect-free structure, a chirality source is placed in the middle of the boundary, and we observe that light propagates unidirectionally along the domain wall, exhibiting strong resistance to backscattering and robust unidirectional transmission. To verify the robustness of the transmission, we introduce defects as shown in Figs. 5(a) and 5(b), representing a cavity and disorder, respectively. The light is not affected by the defects of the cavity and disorder, and it continues to propagate forward. We further test the robustness of the waveguide at bends by constructing domain walls with Z-shaped bends and multiple sharp bends, as shown in Figs. 5(c) and 5(d). Regardless of whether the bend is 60° or 120°, the light does not scatter and lose at the bends, maintaining good transmission.

To numerically verify the effectiveness, we place probes at the beginning and the end of several waveguides to examine the transmission performance and robustness of the waveguides; then, based on the measured energy intensity at the start

and end of the waveguides, we calculate the transmission rate of electromagnetic waves along these boundaries. The calculated transmission coefficients do not include the coupling losses from the source to the waveguide. We only consider transmission rates in the main operational bandwidth (77.2–87 THz). From Fig. 5(e), we observe that the transmission rate for straight waveguides is extremely high, reaching 99.9%, and the cavity and disorder defects have almost no effect on the transmission rate, with only a slight decrease in efficiency at high frequencies (above 86.3 THz), indicating that the range of high-efficiency transmission is narrowed. The Z-shaped and multiple sharp bend waveguides exhibit a decrease in efficiency across the entire operational bandwidth, particularly outside the shaded area in Fig. 5(e), where there is a sharp decline. However, even so, within the shaded frequency band (78.05–86.3 THz) shown in the graph, the transmission rate for Z-shaped waveguides remains above 99%, and for multiple sharp bend waveguides, it is above 97.5%, which still maintains a very high level of transmission.

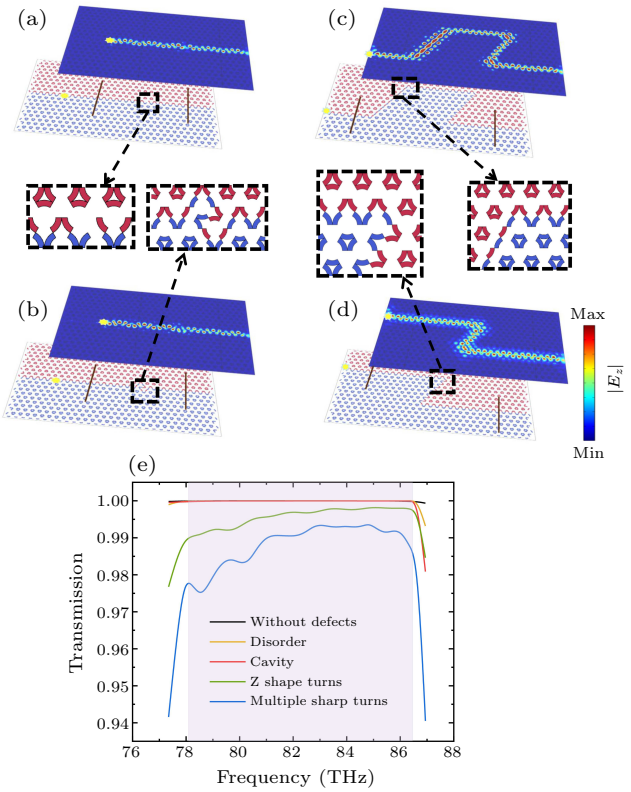


Fig. 5. Construction of defects in the photonic crystal structure composed of VPC1 and VPC2: (a) disorder, (b) cavity, (c) Z-shaped bend, and (d) multiple sharp bends. The electric field patterns formed by chirality source excitation are shown along with the VPC structure diagrams. (e) The graph compares the transmission rates of the defect-free structure with structures that contain disorder, cavity, Z-shaped bend, and multiple sharp bend defects.

This characteristic of enabling electromagnetic waves to pass through defects and sharp bends with high transmission rates can be widely applied in photonic crystal devices, where such robustness ensures the controllability and low power consumption of electromagnetic waves within photonic crystal devices.

We arrange VPC1 and VPC2 into a supercell structure as shown in Fig. 6(a), where the boundary structure is indicated by the black lines in Fig. 6(a), resembling a zipper, which we refer to as a zipper-type structure. The top and bottom boundaries of the supercell still adopt perfect electric conductor boundary conditions, while the left and right boundaries employ periodic boundary conditions. The black dashed lines represent bulk states, and between these bulk states, we can observe edge states formed at the boundaries. The edge modes, shown by the brown solid lines, display the valley pseudospin states of the zipper-like supercell structure. We see that the characteristic frequencies of the edge states are independent of the bulk state characteristic frequencies, implying that the zipper-like boundaries will achieve edge states with good topological protection.

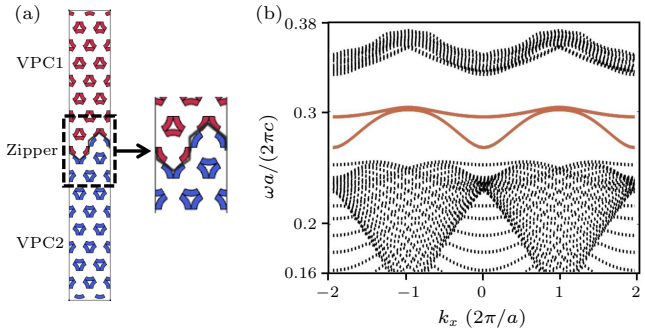


Fig. 6. (a) Supercell structure with zipper-like boundaries. (b) Band structure of a supercell with zipper-type boundaries.

We splice VPC1 and VPC2 together with a zipper-type boundary, and the photonic crystal structure is shown in Fig. 7(b). In Fig. 7(a), a light source is placed at the left end of the boundary. We can observe that the light is well confined and transmits near the boundary. During transmission, the path of light is shown by the Poynting vector in Fig. 7(c). As we can see, there are two electromagnetic waves propagation paths within the zipper-like domain wall, with both paths winding forward. Indeed, due to the edge-1 and edge-2 structures, electromagnetic waves can propagate along 60° sharp bends, maintaining a good transmission rate, thereby forming a zipper-like boundary. The zipper-like boundary is composed of edge-1 and edge-2 configurations. As shown in Fig. 7(d), the edge-2 configuration lies along the diagonal path, and the edge-1 configuration is at the corners. However, after multiple bends, the electromagnetic waves is actually transmitted in a spiral along a straight line (as shown in the Poynting vector diagram), and we can consider it as a straight waveguide.

We examine the transmission rate of the zipper-like boundary and compare it with the transmission rate of the edge-2 boundary. We find that even after passing through waveguides consisting of multiple sharp bends, the zipper-type boundary maintains an extremely high transmission rate

within the 79–90 THz frequency band, nearly identical to that of the straight waveguide structure of the edge-2 configuration. However, there is a decrease in transmission rate below 79 THz and above 90 THz. The operational frequency band for transmission of the zipper-type boundary is completely within the operational frequency bands of both edge-1 type and edge-2 type TESs.

The TESs realized by the zipper-like structure, due to their special propagation characteristics, can propagate at the 90° bends constructed in the transmission waveguides. Compared to the widely known bends of 60° or 120° typically used in photonic crystal beam splitters, our structure's ability to transmit through 90° bends can increase the diversity of photonic crystal waveguide paths. When device design calls for bending waveguides, a 90° bend shortens the transmission path. The new transmission method maintains high transmission rates and robustness while simplifying the structure. These characteristics positively contribute to the expansion and structural tuning of the T-output paths for photonic crystal beam splitters, couplers, and other optical communication devices.

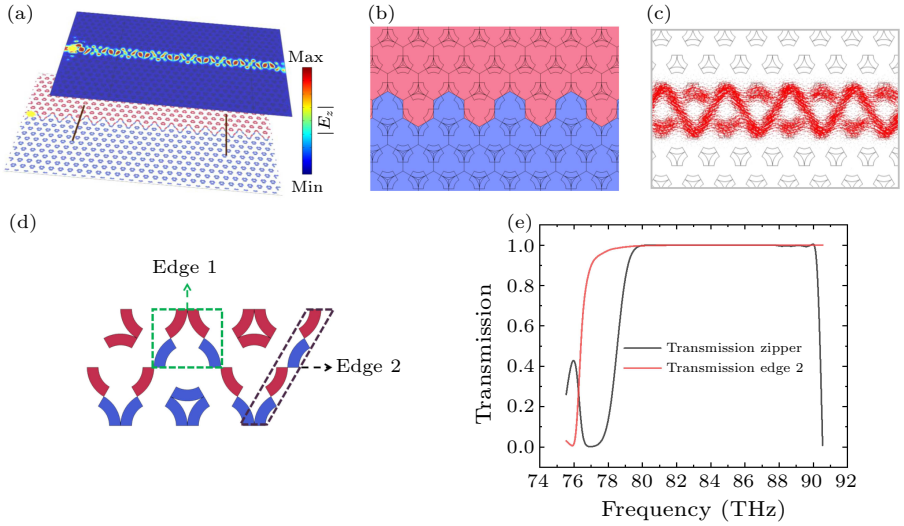


Fig. 7. (a) Photonic crystal (PC) constructed with VPC1 and VPC2 featuring zipper-type boundaries and the simulated E_z field distribution. (b) Schematic diagram of the structure with zipper-type boundaries. (c) Poynting vector diagram when electromagnetic waves transmit through the zipper-like domain wall. (d) Illustration of how edge-1 and edge-2 configurations form the zipper-type boundary. (e) Comparison of the transmission rate of the zipper-type boundary with that of the edge-2 boundary.

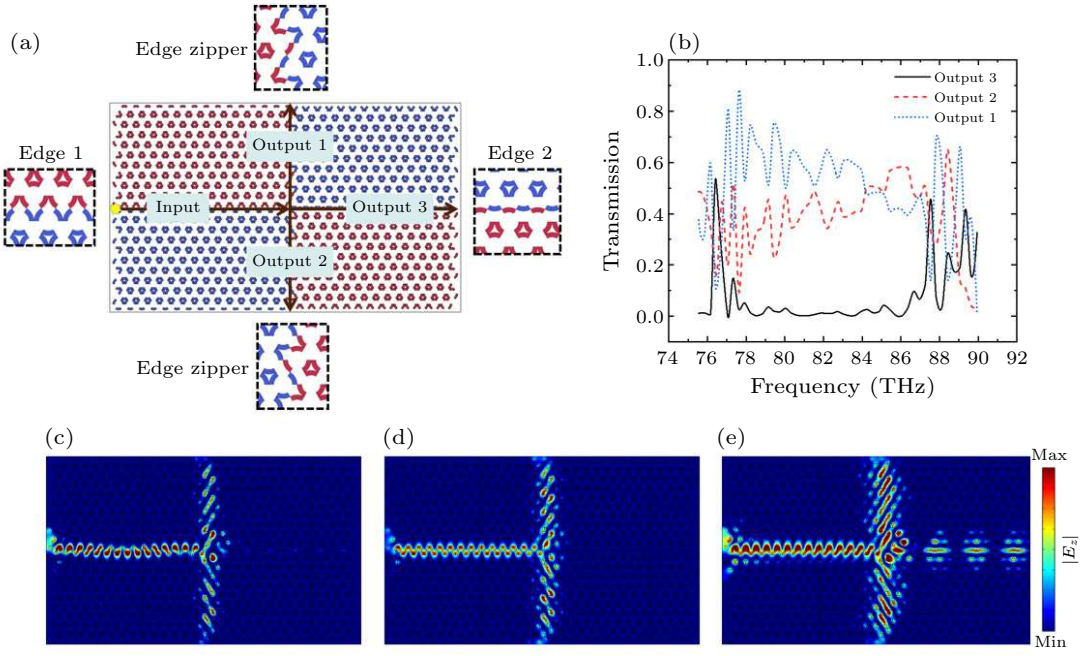


Fig. 8. (a) The structure of the photonic crystal beam splitter constructed with rectangular VPC1 and VPC2. (b) The transmission rates of light in paths of output 1, output 2, and output 3. [(c), (d), (e)] The electric field maps of the device when the input light frequencies are 80.045 THz, 81.544 THz, and 77.946 THz, respectively.

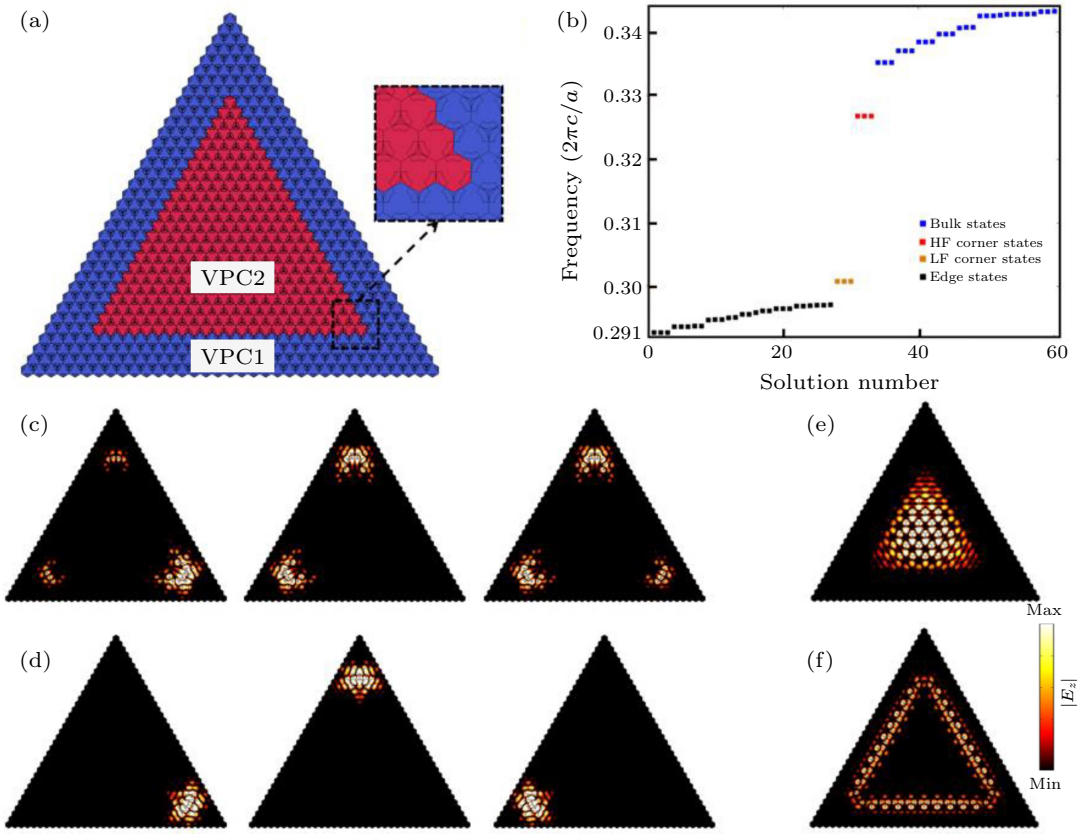


Fig. 9. (a) A box-shaped triangular structure composed of VPC1 and VPC2. The outer structure is VPC1, and the inner structure is VPC2. The boundary between VPC1 and VPC2 is an edge-1 structure. (b) The dispersion diagram corresponding to the box-shaped triangular VPC structure. (c) The E_z field distribution corresponding to LFCSs. (d) The E_z field distribution corresponding to HFCSs. (e) The E_z field distribution corresponding to the bulk states. (f) The E_z field distribution corresponding to the edge states.

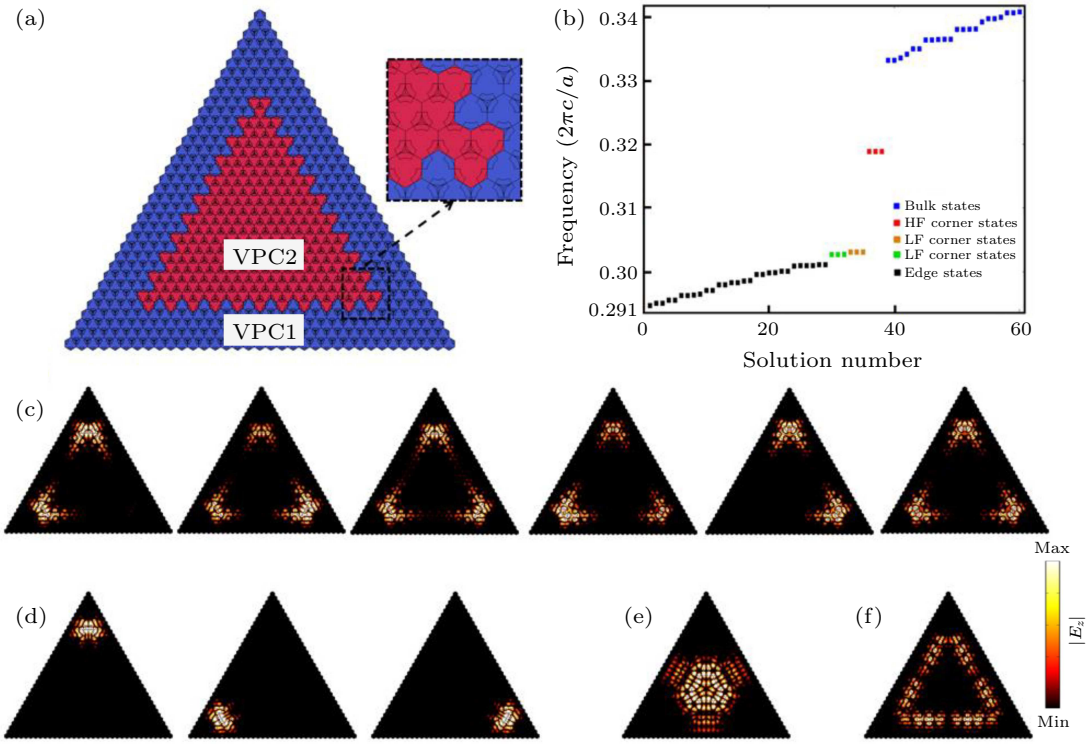


Fig. 10. (a) Box-shaped triangular structure composed of VPC1 and VPC2. The outer layer is VPC1, and the inner layer is VPC2, with a zipper-like boundary structure between VPC1 and VPC2. (b) Characteristic frequencies of the box-shaped triangular structure with zipper-like boundaries. (c) E_z field distribution corresponding to LFCSs. (d) E_z field distribution corresponding to HFCSs. (e) E_z field distribution corresponding to bulk states. (f) E_z field distribution corresponding to edge states.

Based on the characteristics of the TESs realized by the zipper-type boundary, we design a three-output port beam splitter as shown in Fig. 8(a). It has one input channel and three output channels, where output 1 and output 2 both have zipper-type boundaries, the input is an edge-1 type boundary, and output 3 is an edge-2 type boundary. These three types of boundaries can all realize TESs within the working frequency band (76–92 THz) of the device. We place a light source at the input channel as the input end and set probes at the four ports, then calculate the power flow surface density of each reference plane at the working frequency, and derive the transmission coefficients. The transmission rates at the three output ports of the beam splitter are shown in Fig. 8(b). Output 3 has a transmission rate below 3% within the range of 78.3–86.5 THz, within this frequency domain, we can consider that the beam splitter mainly divides the light through output 1 and output 2. Equal energy division is one of the objective standards for evaluating the performance of topological beam splitters. It means that the transmitted energy of output 1 and output 2 reaches an approximately 1:1 ratio, as at 80.045 THz and 81.544 THz the division ratios reach 1:1.05 and 1:1.03, respectively, with the electric fields shown in Figs. 8(c) and 8(d). At frequencies of 76–77.5 THz and 86.5–90 THz, output 3 has a more significant transmission, with transmission rates between 3% and 53%, thereby we can achieve a three-channel output.

Due to the domain wall structure and working frequency band of output-3 path being different from those of output 1 and output 2, its transmission frequency also varies. As known from Fig. 7(b), the transmission rate of output-3 channel is nearly 0 within the range of 78.2–86 THz. Using this property, output 3 effectively isolates the electromagnetic waves in this frequency band, achieving a frequency division effect.

Since we construct a zipper-type boundary, electromagnetic waves can propagate through 90° bends, and the beam splitter can be simply assembled with just rectangular photonic crystal plates. Its assembly is simple with good beam-splitting effects, and the transmission path is short. This minimalist photonic crystal beam splitter offers convenience in real manufacturing compared to traditional beam splitters. Additionally, the device we propose is not easily affected by manufacturing errors such as deformation of the unit cell and defects in the transmission channel such as cavities, disorder, and sharp bends.

4. Topological valley photonic crystal corner states

We know that the existence of gap edge states can lead to formation of corner states, which do not propagate but at certain characteristic frequencies, the energy will be highly localized at the corners of domain walls with topological protection.

In order to verify the presence of corner states, we construct the VPC structure as shown in Fig. 9(a), placing VPC2 as the inner triangle and VPC1 as the outer layer, forming a nested box-shaped triangular VPC structure. The boundary between VPC1 and VPC2 forms an edge-1 boundary, as indicated in Fig. 9(a). The characteristic frequencies obtained from our calculations are displayed in Fig. 9(b), where the black dots represent edge states (TESs), the blue dots represent bulk states, the red dots represent high-frequency corner states (HFCS), and the yellow dots represent low-frequency corner states (LFCS). The characteristic frequency for the HFCS is around 97.955 THz, and for the LFCS, it is near 90.159 THz. The energy of the bulk states is concentrated within the inner triangular VPC2 structure, as shown in Fig. 9(e), while the energy of the edge states is concentrated along the boundary between VPC1 and VPC2, as shown in Fig. 9(f).

Upon analyzing the E_z field distribution of the high-frequency corner states (HFCS), we observe that the energy is predominantly localized at one of the corners of the triangle, and the corners occupied by the TCSs at the three characteristic frequencies do not overlap, as shown in Fig. 9(d). This type of traditional TCS is protected by a generalized chiral symmetry and ideally located on one of the sublattices. On the other hand, the E_z field distribution for the low-frequency corner states (LFCSs) shows that the energy is dispersed over three or two corners of the triangle's boundary, with the intensity gradually diminishing around the corners.

As indicated in the literature,[30] TCSs are widely characterized by both intra-cell coupling and inter-cell coupling. It is the disparity between these two types of coupling that leads to the distinct formations of the high-frequency and low-frequency corner states.

An excess of intra-cell coupling results in the emergence of HFCS, whereas an excess of inter-cell coupling leads to LFCS. Because the three corners of the triangular box structure are surrounded by completely identical configurations, the frequencies of the three TCSs within each set are very close to each other. The difference is negligible on the scale of terahertz (THz), so the three corner states of each set can be approximately regarded as having the same characteristic frequency.

In a similar manner, we arrange VPC1 and VPC2 in a zipper-like configuration to assemble nested box-shaped triangles as shown in Fig. 10(a). The corner structures formed by the zipper-like boundaries differ from the 60° angle structures formed by bending at the edge-1 boundary. We investigate the changes in the TCSs by observing the electric field distribution of this box-shaped structure. Figure 10(b) displays the characteristic frequencies of this box-shaped triangular VPC

structure. Here, the red, brown, and green dots represent corner states, the black dots indicate edge states, and the blue dots represent bulk states. Figures 10(e) and 10(f) show the electric field distributions of edge and bulk states, respectively.

Compared with the TCSs studied earlier, the TCSs of the box-shaped VPC triangle with zipper-like boundaries have an additional set, that is, the low-frequency corner states increase from 1 set to 2. These two sets of LFCSs are similar in form, both decaying slowly at three or two corners, but so less along the path of the boundaries, leading to a slight distribution of energy along the edges. The energy patterns of these LFCSs compared with that of the box-like structure of LFCSs constituted by edge-1 configuration in the previous sections are less localized. We know that at specific frequencies, TESs concentrate energy towards the corners, transiting to TCSs. The LFCSs shown in Fig. 10(c) exhibit characteristics of both TESs and TCSs, akin to a transitional phase between them, which correlates with the characteristic frequencies of the TCSs.

We find that the frequencies of some LFCS are close to the frequencies of edge states, with the approximate characteristic frequencies of the two groups of LFCSs being 90.735 THz and 90.851 THz, respectively, which are close to the characteristic frequency of the nearest TES (90.264 THz). Under these circumstances, the LFCSs represented by the green dots possess some characteristics of edge states, with some energy distributed along the boundaries. Figure 10(c) shows the electric field distribution of the two groups of low-frequency corner states. In contrast, the electric fields of the high-frequency TCSs are ideally confined to the corners. Because their characteristic corner state frequencies are relatively far from the edge and bulk states, as shown in Fig. 10(d), the corner state effect is very pronounced. Conversely, if the characteristic frequencies of the corner states are close to those of bulk or edge states, the energy is dispersed, and the characteristic concentration of energy at the corners of the TCSs is weakened. A stronger localization indicates a higher energy utilization efficiency and reduces the power consumption of the system. To achieve stronger localization of corner states, we should ensure that the characteristic frequencies of the TCSs are far from those of the TESs.

5. Conclusion and perspectives

In summary, we have proposed a quasi-ring-shaped dielectric pillar VPC cell structure that possesses a wide bandgap and disturbance resistance. By breaking the mirror symmetry of the VPC and transforming it from a state of C_{3v} symmetry to C_3 symmetry, we obtain two types of non-trivial monomer VPCs with opened bandgaps, VPC1 and VPC2. We use these two VPC monomers to realize edge states and verify their unidirectional protection and robustness in transmission. Creatively, we construct a zipper-like boundary and achieve high-transmission-rate edge state transmission. Using this kind of edge state, we can construct 90° sharp bends. We apply this zipper-like boundary to a three-output port beam and frequency splitter, which has a good beam splitting and frequency division effect and an extremely simple structure. It can be realized with just a rectangular photonic crystal slab, which is very convenient in practical production. In addition, we construct a triangular box-shaped structure with VPC1 surrounding VPC2. One box-shaped structure uses the edge-1 boundary as the boundary between the VPC1 and VPC2 domains, while the other has a zipper-like boundary. This zipper-like boundary realize a new type of 60° angle structure. We realize two types of corner states, HFCSs and LFCSs, based on these structures. The characteristics of HFCSs and LFCSs are explored in different triangular box-shaped structures. Due to the differentiation of LFCSs, the box-shaped structure with a zipper-like boundary have more TCSs. This shows that the way VPC1 and VPC2 boundaries are stitched together affects the energy distribution pattern of TCSs and changes the characteristic frequencies of TCSs. TCSs close to the characteristic frequencies of TESs gain some energy characteristics of TESs, with reduced localization. This paper explores the transitional nature of TCSs and TESs, explaining the correlation between TCSs characteristic frequencies and localization. This work lays the foundation for designs of integrated photonic devices.

Regarding previous studies on valley photonic crystals, we summarize them. They all utilize regularly shaped scatterers, such as the most classical circular, triangular, and rhombic dielectric pillar valley photonic crystals. In contrast, in this work, we introduce a ring-like structure and innovatively constructed zipper-like boundaries and their applications. This design extends the bandwidth of edge states. Concerning corner states, the zipper-like boundaries can also generate more forms of corner states, showing a broader range of potential applications.

Acknowledgments

Project supported by the Suzhou Basic Research Project (Grant No. SJC2023003) and Suzhou City University National Project Pre-research Project (Grant No. 2023SGY014).

References

[1] Lu L, Joannopoulos J D and Soljačić M 2014 *Nat. Photon.* **8** 821
[2] Hasan M Z and Kane C L 2010 *Rev. Mod. Phys.* **82** 3045
[3] Deng F, Sun Y, Wang X, Xue R, Li Y, Jiang H, Shi Y, Chang K and Chen H 2014 *Opt. Express* **22** 23605
[4] Tzuhsuan M and Gennady S 2017 *Phys. Rev. B* **95** 165102
[5] Dong J W, Chen X D, Zhu H, Wang Y and Zhang X 2017 *Nat. Mater.* **16** 298
[6] Z Yu, H Lin, R Zhou, Z Li, Z Mao, K Peng, Y Liu and X Shi 2022 *J. Appl. Phys.* **132** 163101

[7] Zhao Y L, Liang F, Han J F, Wang X R, Zhao D S and Wang B Z 2022 *Opt. Express* **30** 40515
[8] Ma T and Shvets G 2016 *New J. Phys.* **18** 025012
[9] He X T, Liang E T, Yuan J J, Qiu H Y, Chen X D, Zhao F L and Dong J W 2019 *Nat. Commun.* **10** 872
[10] Chen X D, Zhao F L, Chen M and Dong J W 2017 *Phys. Rev. B* **96** 020202
[11] Shalaev M I, Walasik W, Xu A, Tsukernik Y and Litchinitser N M 2019 *Nat. Nanotechnol.* **14** 31
[12] Gao F, Xue H R, Yang Z J, Lai K F, Yu Y, Lin X, Chong Y D, Shvets G and Zhang B L 2018 *Nat. Phys.* **14** 140
[13] Yang Y H, Yamagami Y, Yu X, Pitchappa P, Webber J, Zhang B, Fujita M, Nagatsuma T and Singh R 2020 *Nat. Photon.* **14** 446
[14] Chen X D, Shi F L, Liu H, Lu J C, Deng W M, Dai J Y, Cheng Q and Dong J W 2018 *Phys. Rev. Appl.* **10** 044002
[15] Makwana M, Craster R and Guenneau S 2019 *Opt. Express* **27** 16088
[16] Wang Z X and Fang Y T 2022 *Physica E* **142** 115240
[17] Zhao Y L, Liang F, Wang X R, Zhao D S and Wang B Z 2022 *J. Phys. D: Appl. Phys.* **55** 155102
[18] Liu J C and Fang Y T 2022 *Physica E* **144** 115451
[19] Wang X R, Fei H M, Lin H, Wu M, Kang L J, Zhang M D, Liu X, Yang Y B and Xiao L T 2023 *Chin. Phys. B* **32** 074205
[20] Wei G C, Liu Z Z, Wu H Z, Wang L C, Wang S X and Xiao J J 2022 *Opt. Lett.* **47** 3007
[21] Wan X, Peng C Y, Li G, Yang J H and Qi X Y 2023 *Chin. Phys. B* **32** 114208
[22] Xu X F, Huang J Y, Zhang H, Guo X Y, Mu S S, Liu Y Q and Zhai N 2021 *Opt. Commun.* **498** 127262
[23] Sui W J, Zhang Y, Zhang Z R, ZhangH F, Shi Q, Lv Z T and Yang B 2023 *Opt. Commun.* **527** 128972
[24] Yao L C, Hsieh K H, Chiu S C, Li H K, Huo S Y and Fu C M 2023 *J. Phys.: Condens. Matter* **35** 205701
[25] Xie B Y, Wang H F, Wang H X, Zhu X Y, Jiang J H, Lu M H and Chen Y F 2018 *Phys. Rev. B* **98** 205147
[26] Hassan A E, Kunst F K, Moritz A, Andler G, Bergholtz E J and Bourennane M 2019 *Nat. Photon.* **13** 697
[27] Serra-Garcia M, Peri V, Susstrunk R, Bilal O R, Larsen T, Villanueva L G and Huber S D 2018 *Nature* **555** 342
[28] Yue Z, Liao D, Zhang Z, Xiong W, Cheng Y and Liu X 2021 *Appl. Phys. Lett.* **118** 203501
[29] Chen X D, Shi F L, Liu J W, Shen K, He X T, Chan C T, Chen W J and Dong J W 2023 *Natl. Sci. Rev.* **10** nwac289
[30] He Y H, Gao Y F, He Y, Qi X F, Si J Q, Yang M and Zhou S Y 2023 *Opt. Laser Technol.* **161** 109196
[31] Phan H T, Liu F and Wakabayashi K 2021 *Opt. Express* **29** 18277
[32] He Y, Gao Y F, Yang M, Yan Z G, He Y H, Qi X F and Liu Z R 2023 *Opt. Mater.* **140** 113830
[33] Shao S, Liang L, Hu J H, Poo Y and Wang H X 2023 *Opt. Express* **31** 17695
[34] O K H and Kim K H 2023 *Photon. Nanostruct. Fundam. Appl.* **54** 101118
[35] Zhang Z S, Li F, Lu J Y, Liu T, Heng X B, He Y C, Liang H H, Gan J L and Yang Z 2020 *Nanophotonics* **9** 2839
[36] Cheng Q, Wang S, Lv J and Liu N 2022 *Opt. Express* **30** 10792
[37] Wu X X, Yan M, Tian J X, Huang Y Z, Hong X, Han D Z and Wen W J 2017 *Nat. Commun.* **8** 1304
[38] Zhao R, Xie G D, Chen M L N, Lan Z H, Huang Z X and Sha W E I 2020 *Opt. Express* **28** 4638
[39] Yang J K, Hwang Y and Oh S S 2021 *Phys. Rev. Res.* **3** L022025